crystals

MDPI

Article

Effect of MnO_2 Concentration on the Conductivity of $Ce_{0.9}Gd_{0.1}Mn_xO_{2-\delta}$

Kerstin Neuhaus [1,*], Stefan Baumann [2], Raimund Dolle [3] and Hans-Dieter Wiemhöfer [1,3]

1 Institute for Inorganic and Analytical Chemistry, University of Münster, Corrensstr. 28/30, 48149 Münster, Germany; hdw@uni-muenster.de
2 Forschungszentrum Jülich GmbH, Institute of Energy and Climate Research, Materials Synthesis and Processing (IEK-1), 52425 Jülich, Germany; s.baumann@fz-juelich.de
3 Helmholtz Institute Münster (HI MS), IEK-12, Forschungszentrum Jülich GmbH, Corrensstraße 46, 48149 Münster, Germany; r.dolle@fz-juelich.de
* Correspondence: kerstin.neuhaus@uni-muenster.de; Tel.: +49-251-83-36095

Received: 15 November 2017; Accepted: 15 January 2018; Published: 17 January 2018

Abstract: Samples with the composition $Ce_{0.9}Gd_{0.1}Mn_xO_{2-\delta}$ with x = 0.01, 0.02, and 0.05 Mn-addition were prepared by mixed oxide route from $Ce_{0.9}Gd_{0.1}O_{2-\delta}$ and MnO_2 and sintered at 1300 °C. The electronic conductivity was measured using a modified Hebb-Wagner technique, the electrical conductivity was investigated by impedance spectroscopy, and oxygen permeation was measured for the sample with x = 0.05. An increase of the electronic partial conductivity with increasing Mn addition was observed, which can be attributed to an additional Mn 3d-related state between the top of the valence band and the bottom of the Ce 4f band. The grain boundary conductivity was found to be suppressed for low Mn contents, but enhanced for the sample with x = 0.05.

Keywords: ceria; Hebb-Wagner measurements; electronic conductivity

1. Introduction

Materials based on doped ceria have been investigated mainly for high temperature applications in solid oxide fuel cells and as sensor materials. In the last ten years, the scientific focus changed from the high temperature regime to application temperatures in the range of room temperature to 400 °C, as ceria has become more and more important in the area of catalytic applications [1–3] (e.g., for the car exhaust catalyst), and also in the pharmaceutical area [4,5]. Manganese doping of ceria has until now been mainly investigated for catalytic applications [1,6] and as additive to improve the sinterability of ceria [7,8]. It has been found additionally that manganese ions are able to diffuse into ceria when it is in contact to Mn containing materials at high temperatures, e.g., during the co-sintering of ceria-perovskite composites for solid oxide fuel cell components. This also caused a certain interest in the effect of Mn doping [7].

So far, the effect of Mn addition has mostly been investigated using Mn as a co-dopant or rather sintering additive [7–10]. Mainly Gd_2O_3 [7,10,11], but in some cases also other oxides [1], were used as main dopants to fix the oxygen vacancy concentration of the material. The solubility limit of Mn in pure ceria has been found to be in the range between 5–10 mol % [7,8,12], or <1 mol % in another study [13]. Also, the solubility was found to be lower in combination with Gd as a co-dopant ($\leq$5 mol %) [12].

The improvement of the sinterability is lower than found for Fe and Co [10,14], but much better than found for Cr addition, which actually inhibits the densification of ceria [15]. Excess Mn, which is not soluble in the ceria matrix, was reported to form the perovskite phase $GdMnO_3$ in combination with Gd [12].

Pikalova et al. [10] and Park et al. [13] reported a decrease in the electrical conductivity for Mn- and Gd-codoped ceria. Apart from this, a change of redox state of Mn^{3+} to Mn^{2+} was found [9,16,17]

for Mn doping in ceria, as well as in yttria stabilized zirconia (YSZ). Sasaki and Maier [17] confirmed a depression of the chemical diffusivity by Mn doping of YSZ because of this redox process, which takes places at roughly $pO_2 = 10^{-5}$ bar at 800 °C. The sintering temperature in literature for Mn doped ceria materials is mainly in the range between 1200 °C and 1300 °C. Previous investigations found that after sintering at temperatures above 1200 °C, manganese ions exist in the divalent state (Mn^{2+}) within the ceria matrix [9]. Therefore, as sintering was performed at ≥1300 °C for the samples presented here, Mn^{3+} and Mn^{4+} should only be present at oxygen partial pressures above the pO_2 of air, which are not addressed in our study.

Theoretical work to corroborate the positive effect on catalytic performance of MnO_x-CeO_2 oxides showed that Mn doping in ceria induces an additional Mn 3d-related gap state between the top of the valence band and the bottom of the Ce 4f band, which facilitates oxygen vacancy formation [16]. This has not yet been verified experimentally. The second aim of this study was to verify whether small amounts of Mn cations work as acceptor dopant or are more or less immiscible within the ceria matrix. Indications for an acceptor doping effect were already found for Fe addition [14,18] and a possible substitution of Ce was also postulated for Mn addition [19], while other studies suggested a low miscibility of Mn within the ceria matrix [13,20]. In case of a low miscibility, Mn-rich segregates could either be found as single defects at the grain boundaries [20] or forming a secondary phase [7,21], which would both influence the grain boundary charge transport characteristics.

Samples with the composition $Ce_{0.9}Gd_{0.1}Mn_xO_{2-\delta}$ with x = 0.01, 0.02, and 0.05 were prepared by the mixed oxide route from $Ce_{0.9}Gd_{0.1}O_{2-\delta}$ and MnO_2. Both, the Mn 3d-related gap states, as well as Mn working as an acceptor dopant in low concentrations, can be verified by the evaluation of the electronic conductivity of Mn doped samples over a broad continuous temperature and oxygen partial pressure range and a comparison of these values to the electrical conductivity. The effect on the grain boundary and bulk conductivity was therefore investigated using impedance spectroscopy in air and the variation of the electronic partial conductivity with varying Mn content was measured using a modified Hebb-Wagner technique. This measurement method permits the temperature dependent detection of the electronic partial conductivity of a sample over a continuous oxygen partial pressure range of roughly 0.21–10^{-20} bar. Additionally, for the sample with x = 0.05, the oxygen permeation was measured to validate the Hebb-Wagner measurements.

2. Materials and Methods

Powders of the composition $Ce_{0.9}Gd_{0.1}Mn_xO_{2-\delta}$ with x = 0.01, 0.02, and 0.05 were synthesized from cerium nitrate hexahydrate ($Ce(NO_3)_3 \cdot 6H_2O$ by abcr, 99.9%), gadolinium nitrate hexahydrate ($Gd(NO_3)_3 \cdot 6H_2O$ by abcr, 99.9%), and manganese dioxide (MnO_2 by Acros Organics, 99%).

Cerium and gadolinium nitrate were dissolved in water, NH_4OH was added until pH = 9 and subsequently H_2O_2 was added dropwise to oxidize Ce^{3+} to Ce^{4+}. The brownish gel was filtered, washed with distilled water, and then dried for 24 h at 70 °C. The resulting powder was then calcined for 4 h at 500 °C in air.

The appropriate amounts of MnO_2 were added. After ball milling for 4 h in ethanol, the powders were dried and then uniaxially dry pressed into pellets. These were sintered subsequently at 1300 °C for 2 h (Mn-containing materials) or at 1600 °C for 4 h (Mn-free reference sample). The samples with 5 mol % Mn, which were applied in the permeation experiments were sintered at 1350 °C for 2 h to achieve sufficient gas-tightness. The grain size of the samples was determined by scanning electronic microscopy using the lineal intercept method [22]. All of the SEM images were obtained in secondary electronic imaging mode with an acceleration voltage of 7 kV and 8 mm working distance.

Impedance measurements in air were carried out as a function of temperature in ambient air using a Novotherm HT 1200 (NovoControl GmbH, Montabaur, Germany). Pt resinate paste (RP 070107, Heraeus GmbH, Hanau, Germany) was applied directly on the sample pellets and was sintered at 850 °C before measurement to minimize any contact resistance. The paste electrodes were contacted by a Pt-sheet. An AC peak-to-peak amplitude of 40 mV was chosen. All the measurements were carried

out in ambient air and in a temperature range from 200–800 °C. The experiments were executed three times at each temperature to control for hysteresis of the conductivity.

The experimental frequency dependence of the impedance was fitted using the software package ZView 2 (Scribner Associates, Inc., Southern Pines, NC, USA) with regard to the medium and high frequency range. For fitting, an equivalent circuit with two resistors in series, which each have a constant phase element (CPE) in parallel, was used [23]. One resistor/constant phase element can be assigned to bulk characteristics and one to grain boundary characteristics, respectively. Figure 1 shows an example of the measured data for pure CGO in the temperature range between 500–200 °C and the equivalent circuit used for evaluation. (σ_b) and grain boundary conductivities (σ_{gb}) have the following connection:

$$R_{total} = R_b + R_{gb} = \frac{n}{A} \cdot \left(\frac{1}{\sigma_b} \cdot L_b + \frac{1}{\sigma_{gb}} \cdot L_{gb} \right) = \frac{1}{\sigma_t} \quad (1)$$

Here, n is the number of grains perpendicular to the electric field, A is the contact area, L_g is the average grain size (cf.), L_{gb} is the average size of the grain boundary, which was in our case assumed to be 1 nm [24,25]. The grain boundary conductivity was corrected with the factor $\frac{L_{gb}}{L_g}$ to calculate the corrected grain boundary conductivity σ^*_{gb}, according to the brick layer model [24,26]. Activation energies were calculated from Arrhenius diagrams of the respective conductivities.

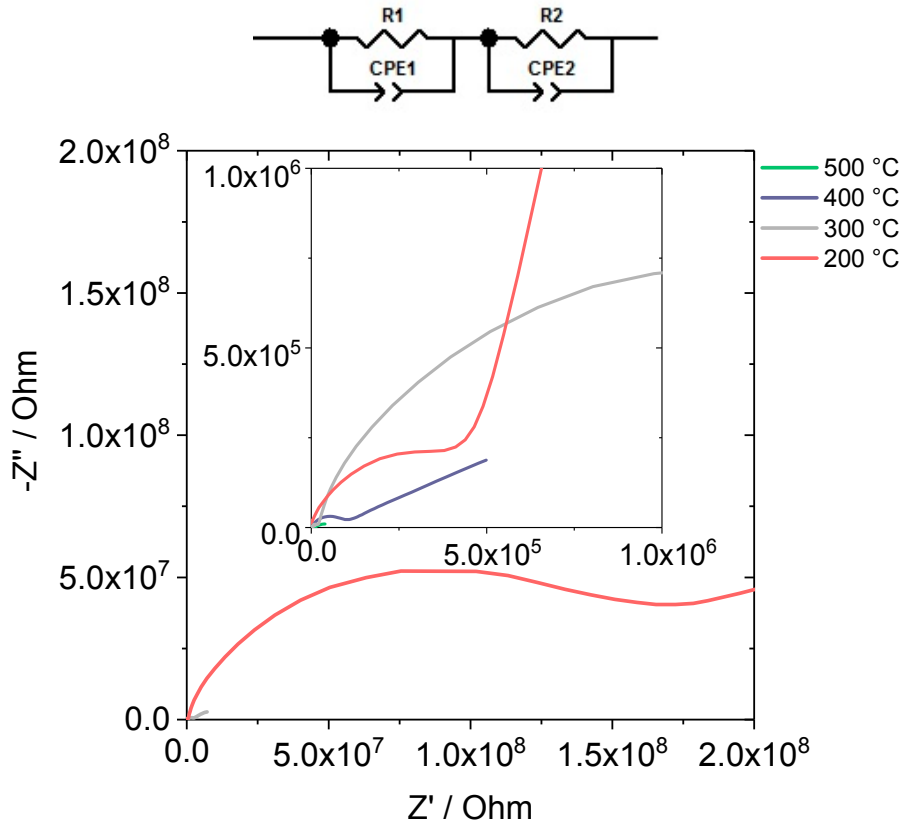

Figure 1. Exemplary impedance spectra for pure CGO at 200−500 °C. Higher temperatures are shown in the inlay. The equivalent circuit used for data evaluation is shown above the graph.

The electronic partial conductivity of the samples was investigated using a home-made modified Hebb-Wagner setup (Sourcemeter: Keithley 2601A, Keithley Instruments, Solon, OH, USA). In this experimental setup, an encapsulated platinum micro contact is applied as working electrode and a Pt sheet as counter electrode. The sample was fixed to the Pt sheet with Pt resinate paste

(RP 070107, Heraeus GmbH). Measurements were carried out at temperatures between 500–800 °C. Each measurement was performed three times and the average value from all three measurements was taken for further calculations.

Permeation experiments were performed on a uniaxially pressed disc 15 mm in diameter sintered at 1350 °C for 2 h in order to achieve sufficient gas-tightness. The thickness of the disc was 0.91 mm after grinding both surfaces with P1200 emery paper. Thin (approx. 5–10 µm) porous surface activation layers of $La_{0.6}Sr_{0.4}Co_{0.2}Fe_{0.8}O_{3-\delta}$ (LSCF) were screen printed on both sides of the disc and calcined at 1050 °C, as described elsewhere [27]. The disc was sealed with two gold rings in an asymmetric glass tube setup. The membrane was heated to 1000 °C, while a spring force was applied to the gold ring sealing. Permeation measurements were carried out between 1000 °C and 400 °C in steps of approx. 50 K with air and argon as feed and sweep gas at a flow rate of 250 and 50 mL/min, respectively. The permeate gas composition was monitored using mass spectrometry (Omnistar, Pfeiffer Vacuum, Asslar, Germany). The nitrogen content in the permeate gas was used to monitor leakage. The nitrogen content in the permeate gas was constantly low (approx. 150 ppm). However, also the concentration of permeated oxygen is very low (<500 ppm), and, hence, the permeation rate was corrected by subtracting 25% of the nitrogen flow rate in the permeate gas from the oxygen flux, reflecting the feed gas composition of approx. 80:20% N_2/O_2. The measurements below 850 °C showed too high leakages, and, hence, were excluded from the investigation.

3. Results

3.1. Microstructure and XRD Measurements

As can be derived from Figure 2, all of the samples were found to be single-phase fluorite materials within limits of detection of the XRD method (limit of detection of crystalline secondary phases is in the area of 3 mol %). The lattice constant of the different samples does not follow a clear trend: 1 and 2 mol % Mn addition lead to an increase of the lattice constant, but measurements for the sample with 5 mol % Mn addition show a decreased lattice constant with respect to the pristine Mn-free material.

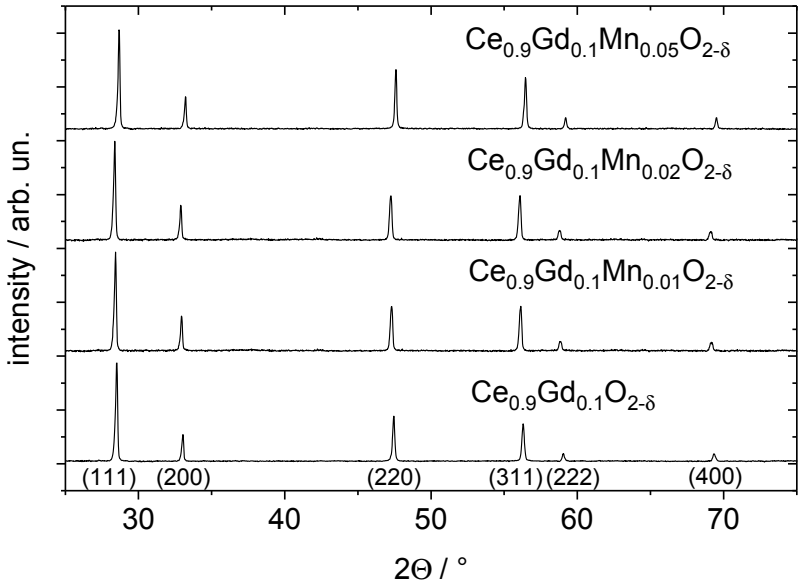

Figure 2. Powder XRD measurements of the four different samples.

As the sintering temperatures and sintering times were different for the Mn-free sample and the three different Mn-containing samples (see Section 2, Materials and Methods), it was already expected that the grain size for the pure CGO10 should be larger than for $Ce_{0.9}Gd_{0.1}Mn_xO_{2-\delta}$ (cf. Table 1 and Figure 3). It can be seen that the average grain size does not follow a clear trend with increasing

Mn addition. The density of the samples with Mn addition is also higher than for the pure CGO10 (cf. Table 1), confirming the findings from literature that addition of small amounts of Mn leads to an improved sinterability.

Table 1. Relative densities calculated from Archimedean balance results and the lattice constants, average grain sizes from microscopic evaluation and measured lattice constants from XRD measurements.

Composition	Density	Average Grain Size	Lattice Constant/Å
x = 0.00	87%	2.6 ± 1.2 µm	5.416
x = 0.01	92%	1.2 ± 0.5 µm	5.432
x = 0.02	88%	1.7 ± 0.7 µm	5.432
x = 0.05	88%	1.4 ± 0.5 µm	5.386

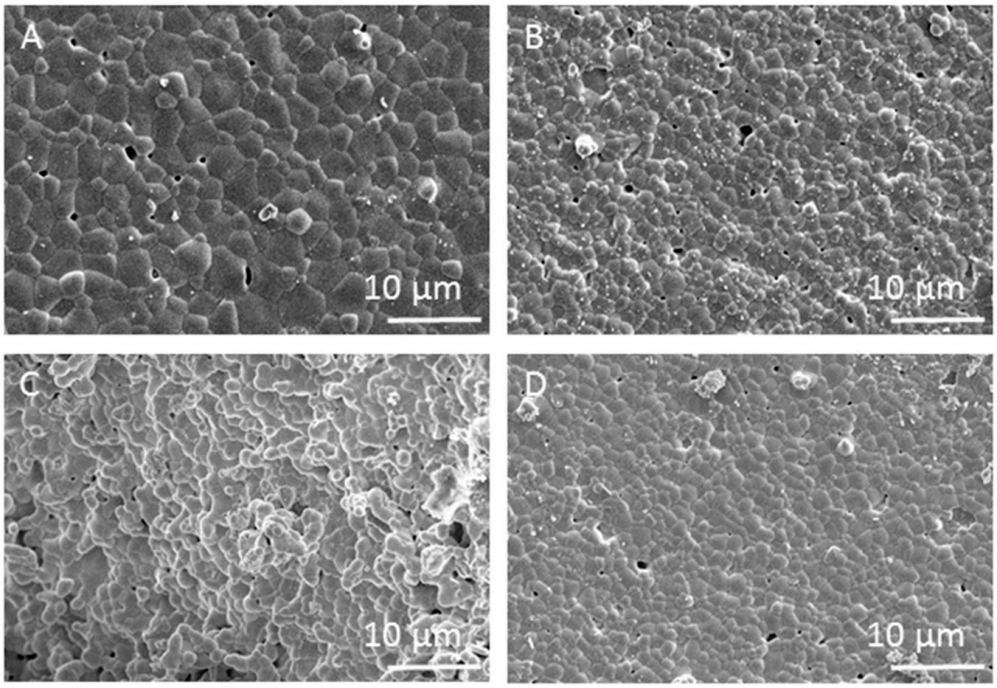

Figure 3. SEM images of the four different samples. (**A**) x = 0.00; (**B**) x = 0.01; (**C**) x = 0.02; and (**D**) x = 0.05.

3.2. Impedance Spectroscopy

It can be observed by comparison of the temperature dependent conductivities presented in Figure 4 that the Mn addition only has a small influence on the electrical conductivity of the samples, which remains in a similar range for all four measured samples, although a slight increase can be observed with increasing Mn addition. This is largely consistent with findings by other groups [10,13].

In contrast, the effect on the grain boundary conductivity is comparably large: a significant drop of σ_{gb}* can be observed for small additions of Mn (x = 0.01 and 0.02) while an addition of 5 mol % Mn leads to a slight increase of the grain boundary conductivity when compared to the pristine CGO10.

Activation energies for the respective transport pathways were calculated from Arrhenius diagrams and for the temperature range of 400–800 °C, as at lower temperatures, a slight decrease of the temperature dependence of the conductivity is visible. The activation energies for grain boundary and total charge transport ($E_{A,gb}$ and $E_{A,tot}$ cf. Table 2) remain in the same range for all of the compositions, while there is a strong variation in the activation energy for bulk transport: for x = 0.01 a pronounced decrease of this values can be found, while for all other compositions, the values remain in a similar range.

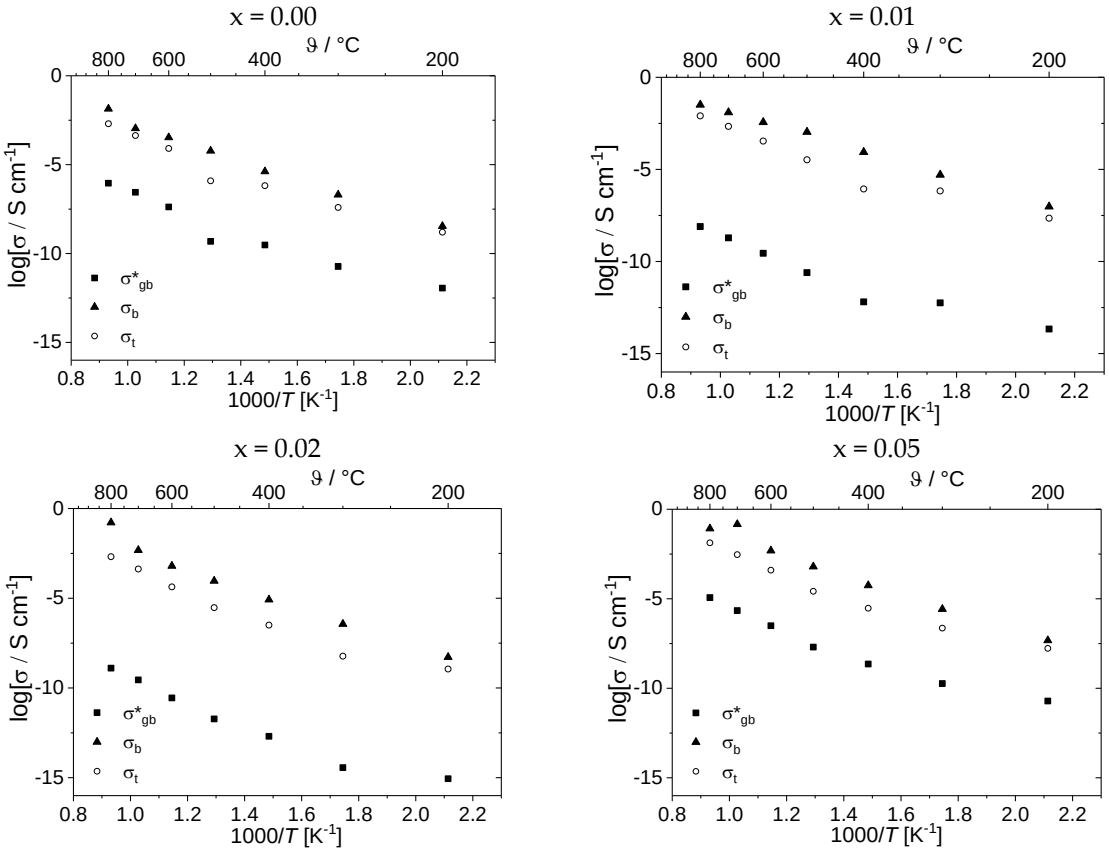

Figure 4. Grain boundary, grain, and electrical conductivity from impedance spectroscopy measurements in air. The grain boundary conductivity was corrected by the factor L_{gb}/L_b.

Table 2. Activation energies for bulk, grain boundary and total transport from impedance spectroscopy measurements in air at 400–800 °C. Standard deviation shows the goodness of the linear fit for calculating the slope of the Arrhenius diagram. The activation energies for hole or electronic transport were calculated from the Hebb-Wagner measurements in chapter 2.3 at pO_2 = 0.21 bar ($E_{A,h}$) or at $pO_2 = 10^{-10}$ bar ($E_{A,e}$), respectively. Values for $Ce_{0.79}Mn_{0.01}Gd_{0.2}O_{2-\delta}$ by Zhang et al. [7] and for $Ce_{0.985}Mn_{0.005}Gd_{0.01}O_{2-\delta}$ by Avila-Paredes et al. [20] are listed for comparison.

Composition	$E_{A,gb}$/eV	$E_{A,bulk}$/eV	$E_{A,tot}$/eV	$E_{A,h}$/eV	$E_{A,e}$/eV
x = 0.00	1.45 ± 0.23	1.26 ± 0.10	1.42 ± 0.21	1.20 ± 0.04	2.24 ± 0.08
x = 0.01	1.51 ± 0.26	0.97 ± 0.04	1.49 ± 0.05	1.00 ± 0.05	2.06 ± 0.09
x = 0.02	1.47 ± 0.08	1.51 ± 0.20	1.47 ± 0.08	1.02 ± 0.03	1.98 ± 0.08
x = 0.05	1.43 ± 0.08	1.34 ± 0.17	1.41 ± 0.07	0.85 ± 0.06	2.15 ± 0.09
$Ce_{0.79}Mn_{0.01}Gd_{0.2}O_{2-\delta}$ [7]	1.03	0.86	1.01	-	-
$Ce_{0.985}Mn_{0.005}Gd_{0.01}O_{2-\delta}$ [20]	1.35 ± 0.03	0.65	-	-	-

The bulk and grain boundary resistances can be utilized to determine the barrier function of the grain boundaries with respect to ionic diffusion, assuming a phase-pure material. Acceptor doped ceria grains were previously described by a space charge model, where the grain boundaries present a Mott-Schottky type contact [28]. Hence, the electrostatic (or space charge) potential barrier $\Delta\varphi_s$, which is equivalent to the Schottky barrier height, can be calculated from the impedance spectroscopy measurements by solving the following equation numerically [20]:

$$\frac{\rho_{gb}}{\rho_{bulk}} = \frac{\exp\left(\frac{2e\Delta\varphi_s}{kT}\right)}{\frac{4e\Delta\varphi_s}{kT}} \quad (2)$$

Here, ρ_{gb} is the grain boundary resistivity, ρ_{bulk} is the bulk resistivity, e is the elementary charge, k is the Boltzmann constant in J/K, and T is the absolute temperature in K [20]. The space charge potential difference can be equated to the grain boundary core potential:

$$\Delta\varphi_s = \varphi_s - \varphi_{bulk} \quad (3)$$

Avila-Paredes et al. [20] calculated the grain boundary core potential for the composition $Ce_{0.985}TM_{0.005}Gd_{0.01}O_{2-\delta}$ (TM = Co, Fe, Cu, and Mn) and found potentials in the area of $\Delta\varphi_s$ = 0.4 to 0.55 V. This is roughly two times higher than the values found in our study (cf. Figure 5), but the space charge potential barrier is heavily dependent on grain size [29] and dopant distribution.

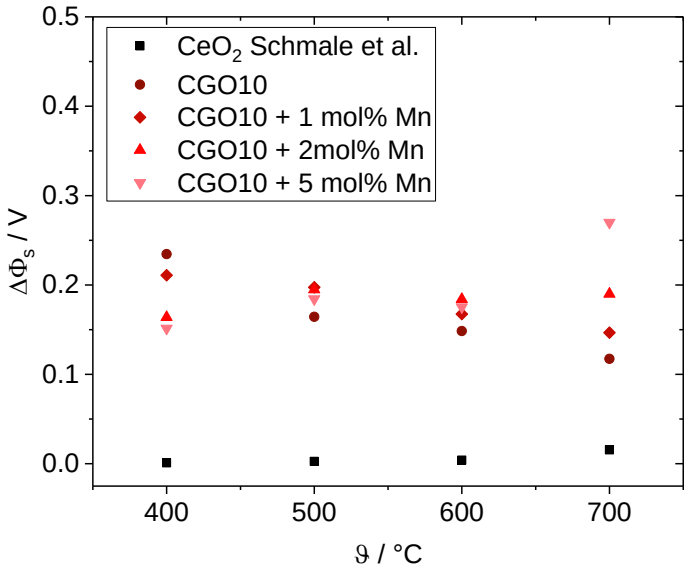

Figure 5. Temperature dependence of the space charge potential of $Ce_{0.9-x}Gd_{0.1}MnxO_{2-\delta}$ in comparison to nominally pure ceria (99.9% purity) [23] calculated by Equation (2).

When comparing the values for pure CeO_2 by [23] to the values for $Ce_{0.9}Gd_{0.1}Mn_xO_{2-\delta}$, it can be seen that Gd doping leads to an increase of the space charge potential barrier at the grain boundaries of ceria. The effect is more intense for low temperatures and decreases with increasing temperature. The influence of Mn differs: at high temperatures, Mn addition leads to an increase of the barrier height, while at low temperatures, a decreasing effect can be observed as compared to pristine CGO10.

3.3. Electronic Conductivity

By applying an electrical potential difference (potential V_{exp} in Figure 6) to the cell, the oxygen partial pressure at the microcontact can be controlled under steady-state conditions. The oxygen partial pressure at the microcontact (denoted by $pO_{2,cont}$) is given with respect to the reference partial pressure of air at the large planar back contact by the Nernst Equation:

$$V_{exp} = \frac{RT}{4F} ln\left[\frac{pO_{2,\,cont}}{pO_{2,\,air}}\right] + V_{cont} \quad (4)$$

The sign of the applied potential V_{exp} refers to the polarity of the microcontact. Only negative potentials were applied, i.e., $pO_{2,cont} < pO_{2,air}$. An oxygen partial pressure that significantly exceeds the pressure of air leads to a breakdown of the glass encapsulation due to formation of gas bubbles. Oxygen partial pressures above 0.21 bar were therefore not addressed in this study.

The non-negligible ohmic contact resistance R_{cont} of the interface between sample and microcontact is considered by addition of the voltage V_{cont} in (4). As V_{cont} is variable with temperature

and applied voltage, it has not been corrected in these measurements. This leads to an underestimation of the measured electronic conductivities presented in this study.

The oxygen partial pressure at the microcontact is given by

$$pO_{2,\,\mathrm{cont}} = 0.21\ \mathrm{bar} \cdot \exp\left[\frac{4F(V_{\mathrm{exp}} - V_{\mathrm{cont}})}{RT}\right] \tag{5}$$

with R = gas constant, T = temperature in K, and F = Faraday constant. In accordance with the Hebb-Wagner model, the local electronic conductivity (σ_e) of the ceria sample at the ion-blocking microelectrode can be calculated by multiplying the slope of the steady-state potential curve (see exemplary experimental I-V curve in Figure 6) with a geometric factor considering the radius of the tip. For a flat, disk shaped platinum tip, σ_e as a function of the local oxygen partial pressure at the microcontact is obtained by:

$$\sigma_e(pO_{2,\,\mathrm{cont}}) = \left(\frac{\delta I}{\delta V}\right)_{\mathrm{st}} \cdot \frac{1}{2\pi a} \tag{6}$$

The index 'st' of the derivative denotes that values are obtained from the steady state I-V curve. For each data point, the respective voltage was held for 30 min in the temperature range between 600–800 °C or 45 min for all measurements below 600 °C, before the average value of the steady state current was determined. As "abort criterion" to minimize the measurement time, the polarization was considered complete (and the steady state reached) if the value of the measured current did not change more than 0.5% over a time of 180 s (240 s at temperatures below 600 °C). All of the electronic conductivity values were corrected for the microcontact diameter, which was determined by measuring the contact print in the glass encapsulation after the end of the measurement. The diameter of the contact area was in the range between 220–330 µm for the various experiments.

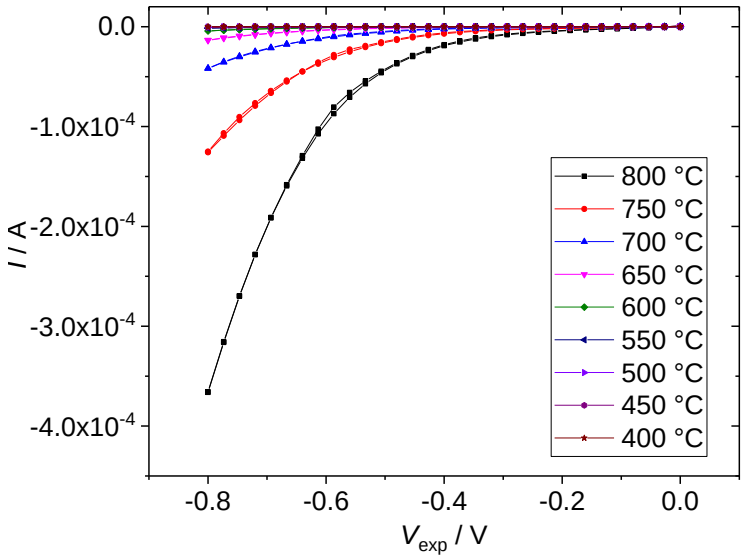

Figure 6. Experimental I-V curves for one Hebb-Wagner experiment for the sample with the composition $Ce_{0.9}Gd_{0.1}Mn_{0.01}O_{2-\delta}$.

As can be seen from Figure 7, a significant increase of the electronic conductivity was found for Mn-doped materials in comparison with pristine CGO10. At the same time, the position of the minimum of electronic conductivity remains at the same oxygen partial pressure.

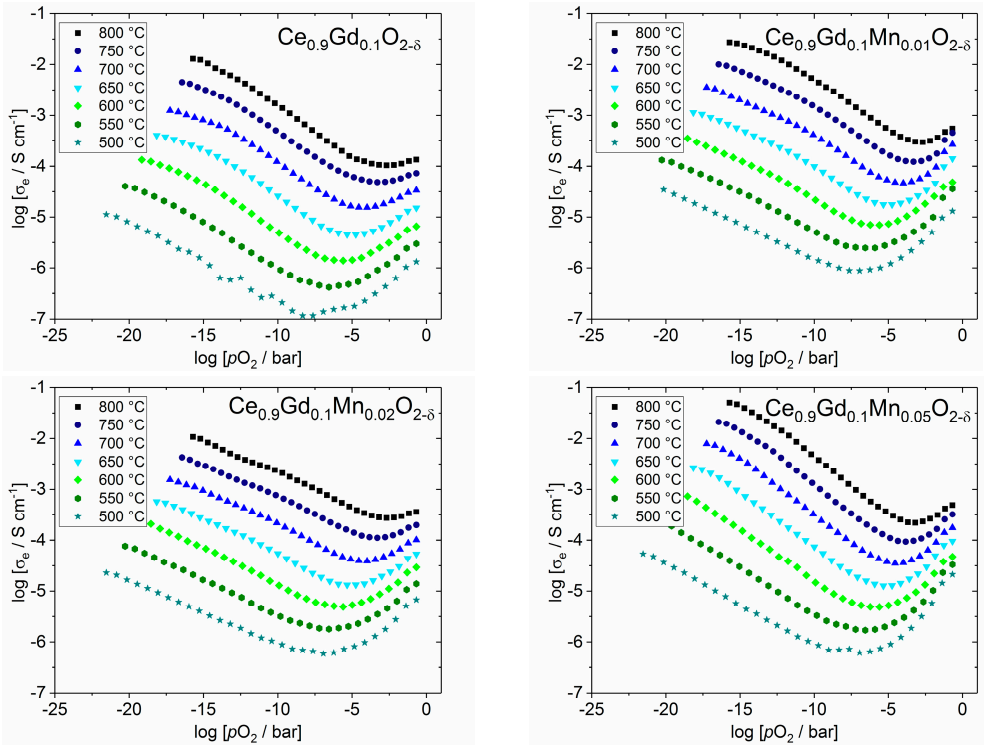

Figure 7. Oxygen partial pressure dependent conductivity for the four different samples. Average error for each point is ≤4%. The values were corrected for the microcontact diameter, but not for contact resistance. Indication for ± 1/4 and ± 1/6 slopes are given in each graphic.

In Figure 8, the electronic conductivities for the respective samples at pO_2 = 0.21 bar and $pO_2 = 10^{-10}$ bar are plotted. It can be observed that the p-type conduction at 0.21 bar is significantly enhanced, and also the activation energy for charge transfer ($E_{A,h}$), which was calculated for this partial pressure range (cf. Table 2) shows a significant decrease with increasing Mn addition.

For the lower oxygen partial pressure, this is not the case: here, the activation energies ($E_{A,e}$ in Table 2) are significantly lowered for the addition of 1 and 2 mol % Mn but get back to a similar value for 5 mol % Mn addition. Also, the activation energies for p-type charge transport ($E_{A,h}$) are by a factor of 2 lower than for n-type charge transport ($E_{A,e}$) for all samples in this study.

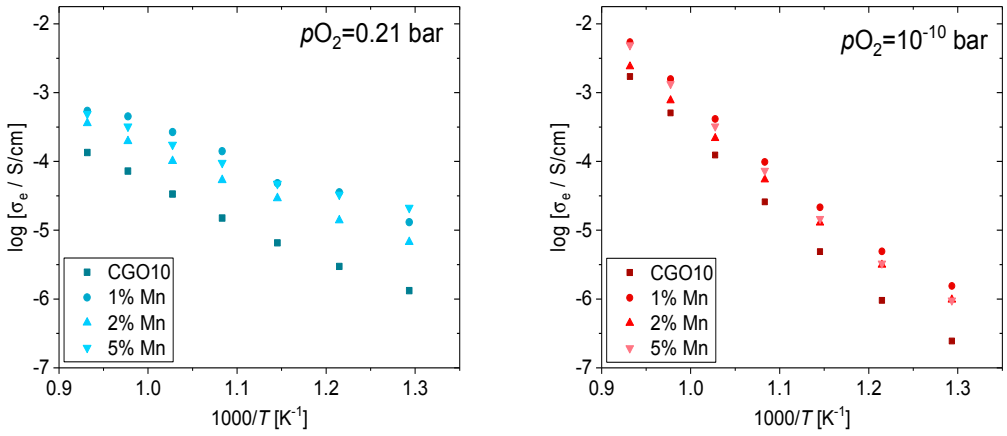

Figure 8. Electronic conductivity at pO_2 = 0.21 bar (blue symbols) and at $pO_2 = 10^{-10}$ bar (red symbols) for the respective compositions. A list of activation energies for electronic transport at these partial pressures can be found in Table 2.

3.4. Oxygen Permeation

The oxygen permeation rate j_{O_2} can be described using the simplified Wagner equation (Equation (4)), assuming that the ambipolar conductivity is independent of oxygen partial pressure within the gradient between feed and permeate side.

$$j_{O_2} = \frac{R}{16F^2} \cdot \frac{1}{L} \cdot \sigma_{amb} T \cdot \ln \frac{p'_{O_2}}{p''_{O_2}} \quad (7)$$

R is the gas constant, F is the Faraday constant, L is the membrane thickness, σ_{amb} is the ambipolar conductivity, T is the absolute temperature, and p'_{O2} and p''_{O2} are the oxygen partial pressures at the feed and permeate side, respectively. σ_{amb} is composed of the ion conductivity σ_i and the electronic conductivity σ_e and can also be expressed by the ionic end electronic transference numbers t_i and t_e, respectively (Equation (8)).

$$\sigma_{amb} = \frac{\sigma_i \cdot \sigma_e}{\sigma_i + \sigma_e} = t_i t_e \sigma_t \quad (8)$$

In contrast to other mixed ionic electronic conducting materials, such as $La_{0.6}Sr_{0.4}Co_{0.2}Fe_{0.8}O_{3-\delta}$ (LSCF), where the electronic conductivity is orders of magnitude larger compared to the ion conductivity [30], Mn co-doped CGO has the opposite properties, i.e., $\sigma_e << \sigma_i$. With this boundary condition, σ_e can be calculated and plotted versus the electrical conductivity, as shown in Figure 9. The slope of the linear regression gives an average of the electronic transference of 0.009. The calculated electronic conductivities at high temperature are in very good agreement to those extrapolated from values of the Hebb-Wagner-method at lower temperatures, as shown in Figure 10. The oxygen permeation measurement also prove, that the Hebb-Wagner polarization experiments yield consistent data, as the density of the samples (see Table 1) was relatively low and Hebb-Wagner experiments should normally only be performed for samples with a high density (≥95%).

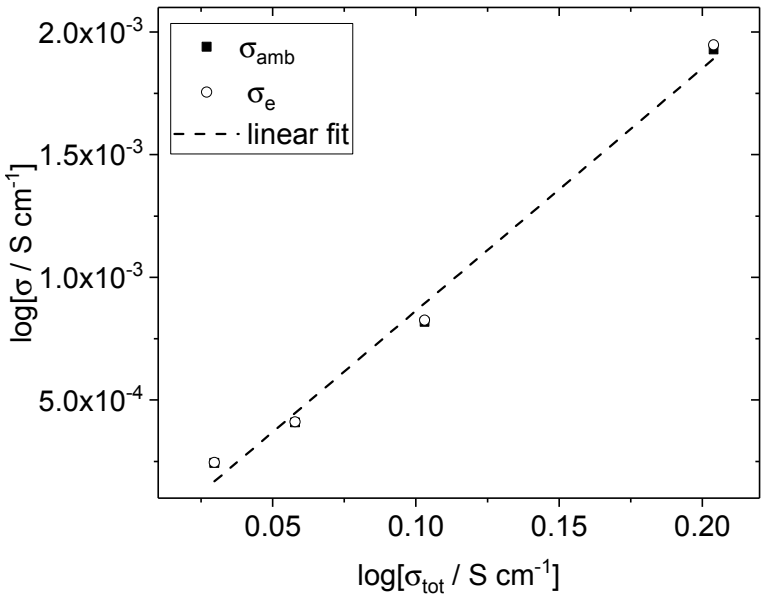

Figure 9. Electronic conductivity calculated via Equations (6) and (7) as function of electrical conductivity determined by impedance spectroscopy.

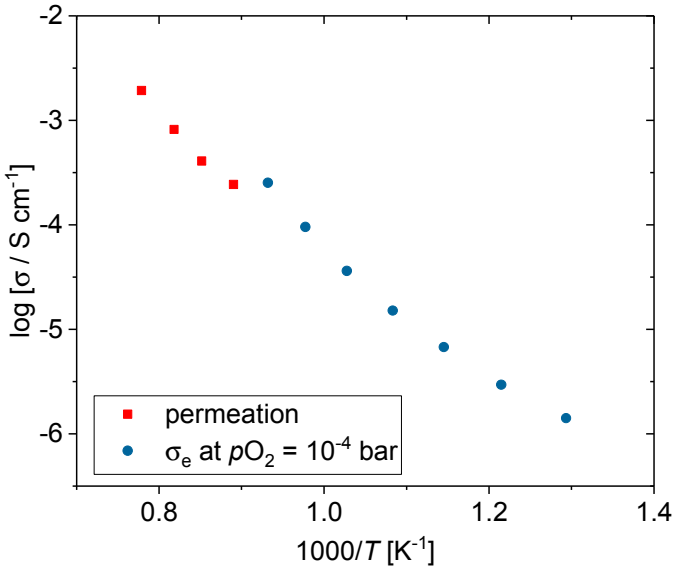

Figure 10. Electronic conductivities determined by oxygen permeation (red) and Hebb-Wagner measurements (blue).

4. Discussion

The lattice constant of CGO with Mn-addition presented in Section 3.1 did not show a clear trend. A lattice expansion with Mn addition could be taken as hint for Mn in interstitial positions in the ceria structure at least for 1 and 2 mol % Mn addition. Mn^{2+} has a similar ionic radius (91 pm) like Ce^{4+}, but substitution of Ce^{4+} therefore would not lead to a lattice expansion. Still, this scenario does not explain the decrease of the lattice constant for x = 0.05. A possible explanation could be, that after reaching a certain Mn threshold concentration, a secondary phase is formed (formation of $GdMnO_3$ has already been observed for Mn-addition to highly Gd-doped ceria [12]), which incorporates most of the Mn, but this cannot be verified with the data measured in this study.

In our electrochemical measurements, a strong effect of Mn addition on the grain boundary conductivity has been observed, with 1 and 2 mol % Mn addition, leading to a significant decrease of the grain boundary conductivity. In contrast, a substantial increase was found for 5 mol % Mn addition when compared to the pristine CGO10. This further substantiates the idea of the segregation of Mn as a second phase at the grain boundaries.

The observed strong increase of the electronic conductivity without any change of the position of the conductivity minimum in dependence on oxygen partial pressure confirms the assumption that Mn doping leads to an additional Mn 3d-related state between the top of the valence band and the bottom of the Ce 4f band [16]. In addition, in the low temperature regime a lowered potential barrier $\Delta\varphi_s$ between grains and grain boundaries, which was found with increasing Mn concentration, could also improve the electronic transport between grains.

The constant position of the minimum of the electronic conductivity can however only be taken as hint that Mn does neither work as a donor or acceptor dopant within the ceria matrix, because the defect chemistry of the material is already strongly influenced by the Gd co-dopant. As no additional maximum of the electronic conductivity was found in the oxygen partial pressure range between 10^{-4} and 10^{-7} bar [17] (which would be the case if predominantly trivalent or tetravalent Mn was existing in the samples and would be reduced during Hebb-Wagner measurements), Mn exists predominantly in a Mn^{2+} state, as initially assumed [9]. Reduction of Mn^{3+} or Mn^{4+} would hypothetically lead to a small polaron hopping process, which could be comparable to the effect of the reduction process of $Pr^{3+/4+}$ [31], but this mechanism was not observed.

By comparing electronic and electrical conductivity in the high temperature regime (cf. Table 3), we can ascertain that Mn addition has only a minor effect for 700–800 °C, while for lower temperatures, the electronic transport in slightly Mn doped materials becomes more prominent. The strongest effect can be observed for 1 mol% Mn addition. For 2 and 5 mol%, a behavior that is comparable to pristine CGO10 can be found. Permeation measurements confirmed the electronic conductivity data from Hebb-Wagner measurements for 5 mol% Mn addition.

Table 3. Electronic transference numbers t_e for the different samples at chosen temperatures. Data for 900 and 1000 °C were determined from permeation measurements.

$Ce_{0.9}Gd_{0.1}Mn_xO_{2-\delta}$	600 °C	700 °C	800 °C	900 °C	1000 °C
x = 0	0.41	0.17	0.07	-	-
x = 0.01	0.78	0.11	0.07	-	-
x = 0.02	0.39	0.14	0.10	-	-
x = 0.05	0.45	0.11	0.04	0.007	0.010

An enhanced influence of Mn at lower temperature can also be found regarding the potential barrier at the grain boundaries: at high temperatures, Mn addition increases the grain boundary core potential by roughly a factor of 2.5 with respect to the bulk potential, while at low temperatures a decreasing effect (about 40% lower) can be observed when compared to pristine CGO10. This behavior is especially pronounced for 5 mol% Mn addition.

Two possible options can be the cause for this effect: on the one hand, the contrarious temperature dependence of the grain boundary potential barrier with respect to pure CGO could be caused by a Mn-rich second phase at the grain boundaries. Such an effect was already confirmed for secondary phases formed by Fe addition to ceria [18], and secondary phase formation ($GdMnO_3$) was already observed for Mn addition to heavily Gd-doped ceria [12]. Such a secondary phase does not necessarily appear in the XRD measurements, as it could either have a concentration below the detection limit of XRD or it could be amorphous. Alternatively, the effect on the grain boundary potential barrier could also be triggered by a local increase of the Mn^{2+} concentration and a parallel depletion of segregated Gd^{3+} at the grain boundaries. Both of the effects could potentially occur at the same time.

In conclusion, an impact on the electronic partial conductivity, even of small amounts of Mn was detected. This can on the one hand be mainly attributed to Mn introducing additional states in the ceria band gap, which facilitates electronic transport. On the other hand, a reduced potential barrier at the grain boundaries, which was found to decrease for increasing Mn content for temperatures below 500 °C, can also facilitate electronic transport. A clear indication for a donor (Mn on the interstitial lattice sites as proposed by XRD measurements) or acceptor doping effect (Mn substituting for Ce as initially thought) was not discernible from the electrochemical measurements or the XRD data. This is consistent with findings by Park et al. [13].

Altogether, this means, that for example co-sintering of ceria and Mn-containing materials will lead to slightly changed characteristics of the ceria phase itself. A detailed TEM-based analysis of the grain boundaries could additionally show, whether the lowered potential barrier at low temperatures for the sample with 5 mol % Mn content can be ascribed to secondary phase formation or to a lowered Gd^{3+} segregation at the grain boundaries. Both of the effects could be exploited to tailor the grain boundary characteristics of ceria-based composite materials for particular low temperature applications by carefully manipulating the Mn concentration within the material.

Acknowledgments: Many thanks to S. Heinz for sample preparation and execution of the oxygen permeation tests. Investigations were performed during preliminary studies for a collaborative project funded by the German Research Foundation—project number 387282673.

Author Contributions: K.N. and S.B. conceived and designed the experiments; K.N. and S.B. performed the experiments; K.N. and S.B. analyzed the data; R.D. and H.D.W. contributed to the analysis and discussion; K.N. wrote the paper.

Conflicts of Interest: The authors declare no conflict of interest. The founding sponsors had no role in the design of the study; in the collection, analyses, or interpretation of data; in the writing of the manuscript, and in the decision to publish the results.

References

1. Terribile, D.; Trovarelli, A.; de Leitenburg, C.; Primavera, A.; Dolcetti, G. Catalytic combustion of hydrocarbons with Mn and Cu-doped ceria–zirconia solid solutions. *Catal. Today* **1999**, *47*, 133–140. [CrossRef]
2. Yao, H.C.; Yao, Y.F.Y. Ceria in automotive exhaust catalysts: I. Oxygen storage. *J. Catal.* **1984**, *86*, 254–265. [CrossRef]
3. Trovarelli, A. Catalytic properties of ceria and CeO_2-containing materials. *Catal. Rev.* **1996**, *38*, 439–520. [CrossRef]
4. Tarnuzzer, R.W.; Colon, J.; Patil, S.; Seal, S. Vacancy engineered ceria nanostructures for protection from radiation-induced cellular damage. *Nano Lett.* **2005**, *5*, 2573–2577. [CrossRef] [PubMed]
5. Wason, M.S.; Zhao, J. Cerium oxide nanoparticles: Potential applications for cancer and other diseases. *Am. J. Transl. Res.* **2013**, *5*, 126–131. [PubMed]
6. Mandal, S.; Santra, C.; Bando, K.K.; James, O.O.; Maity, S.; Mehta, D.; Chowdhury, B. Aerobic oxidation of benzyl alcohol over mesoporous Mn-doped ceria supported au nanoparticle catalyst. *J. Mol. Catal. A* **2013**, *378*, 47–56. [CrossRef]
7. Zhang, T.; Kong, L.; Zeng, Z.; Huang, H.; Hing, P.; Xia, Z.; Kilner, J. Sintering behavior and ionic conductivity of $Ce_{0.8}Gd_{0.2}O_{1.9}$ with a small amount of MnO_2 doping. *J. Sol. State Electrochem.* **2003**, *7*, 348–354. [CrossRef]
8. Zhang, T.; Hing, P.; Huang, H.; Kilner, J. Sintering study on commercial CeO_2 powder with small amount of MnO_2 doping. *Mater. Lett.* **2002**, *57*, 507–512. [CrossRef]
9. Tianshu, Z.; Hing, P.; Huang, H.; Kilner, J. Sintering and densification behavior of Mn-doped CeO_2. *Mater. Sci. Eng. B* **2001**, *83*, 235–241. [CrossRef]
10. Pikalova, E.Y.; Demina, A.N.; Demin, A.K.; Murashkina, A.A.; Sopernikov, V.E.; Esina, N.O. Effect of doping with Co_2O_3, TiO_2, Fe_2O_3, and Mn_2O_3 on the properties of $Ce_{0.8}Gd_{0.2}O_{2-\delta}$. *Inorg. Mater.* **2007**, *43*, 735–742. [CrossRef]
11. Kondakindi, R.R.; Karan, K. Characterization of Fe- and Mn-doped GDC for low-temperature processing of solid oxide fuel cells. *Mater. Chem. Phys.* **2009**, *115*, 728–734. [CrossRef]
12. Kang, C.Y.; Kusaba, H.; Yahiro, H.; Sasaki, K.; Teraoka, Y. Preparation, characterization and electrical property of Mn-doped ceria-based oxides. *Solid State Ion.* **2006**, *177*, 1799–1802. [CrossRef]
13. Park, S.-H.; Yoo, H.-I. Defect-chemical role of Mn in Gd-doped CeO_2. *Solid State Ion.* **2005**, *176*, 1485–1490. [CrossRef]
14. Fagg, D.P.; Kharton, V.V.; Frade, J.R. P-type electronic transport in $Ce_{0.8}Gd_{0.2}O_{2-\delta}$: The effect of transition metal oxide sintering aids. *J. Electroceram.* **2002**, *9*, 199–207. [CrossRef]
15. Taub, S.; Neuhaus, K.; Wiemhöfer, H.-D.; Ni, N.; Kilner, J.A.; Atkinson, A. The effects of Co and Cr on the electrical conductivity of cerium gadolinium oxide. *Solid State Ion.* **2015**, *282*, 54–62. [CrossRef]
16. Cen, W.; Liu, Y.; Wu, Z.; Wang, H.; Weng, X. A theoretic insight into the catalytic activity promotion of CeO_2 surfaces by Mn doping. *Phys. Chem. Chem. Phys.* **2012**, *14*, 5769–5777. [CrossRef] [PubMed]
17. Sasaki, K.; Maier, J. In situ EPR studies of chemical diffusion in oxides. *Phys. Chem. Chem. Phys.* **2000**, *2*, 3055–3061. [CrossRef]
18. Tsipis, E.V.; Waerenborgh, J.C.; Kharton, V.V. Grain-boundary states in solid oxide electrolyte ceramics processed using iron oxide sintering aids: A Mössbauer spectroscopy study. *J. Solid State Electrochem.* **2017**, *21*, 2965–2974. [CrossRef]
19. Pereira, G.J.; Castro, R.H.R.; de Florio, D.Z.; Muccillo, E.N.S.; Gouvêa, D. Densification and electrical conductivity of fast fired manganese-doped ceria ceramics. *Mater. Lett.* **2005**, *59*, 1195–1199. [CrossRef]
20. Avila-Paredes, H.J.; Kim, S. The effect of segregated transition metal ions on the grain boundary resistivity of gadolinium doped ceria: Alteration of the space charge potential. *Solid State Ion.* **2006**, *177*, 3075–3080. [CrossRef]
21. Foschini, C.R.; Souza, D.P.F.; Paulin Filho, P.I.; Varela, J.A. Ac impedance study of Ni, Fe, Cu, Mn doped ceria stabilized zirconia ceramics. *J. Eur. Ceram. Soc.* **2001**, *21*, 1143–1150. [CrossRef]

22. Wurst, J.C.; Nelson, J.A. Lineal intercept technique for measuring grain size in two-phase polycrystalline ceramics. *J. Am. Ceram. Soc.* **1972**, *55*, 109. [CrossRef]
23. Schmale, K.; Daniels, M.; Buchheit, A.; Grünebaum, M.; Haase, L.; Koops, S.; Wiemhöfer, H.-D. Influence of zinc oxide on the conductivity of ceria. *J. Electrochem. Soc.* **2013**, *160*, F1081–F1087. [CrossRef]
24. Jasper, A.; Kilner, J.A.; McComb, D.W. TEM and impedance spectroscopy of doped ceria electrolytes. *Solid State Ion.* **2008**, *179*, 904–908. [CrossRef]
25. Hwang, J.-H.; McLachlan, D.S.; Mason, T.O. Brick layer model analysis of nanoscale-to-microscale cerium dioxide. *J. Electroceram.* **1999**, *3*, 7–16. [CrossRef]
26. Christie, G.M.; Van Berkel, F.P.F. Microstructure—Ionic conductivity relationships in ceria-gadolinia electrolytes. *Solid State Ion.* **1996**, *83*, 17–27. [CrossRef]
27. Ramasamy, M.; Persoon, E.S.; Baumann, S.; Schroeder, M.; Schulze-Küppers, F.; Görtz, D.; Bhave, R.; Bram, M.; Meulenberg, W.A. Structural and chemical stability of high performance $Ce_{0.8}Gd_{0.2}O_{2-\delta}$-$FeCo_2O_4$ dual phase oxygen transport membranes. *J. Membr. Sci.* **2017**, *544*, 278–286. [CrossRef]
28. Kim, S.; Maier, J. On the conductivity mechanism of nanocrystalline ceria. *J. Electrochem. Soc.* **2002**, *149*, J73–J83. [CrossRef]
29. Wang, B.; Lin, Z. A schottky barrier based model for the grain size effect on oxygen ion conductivity of acceptor-doped ZrO_2 and CeO_2. *Int. J. Hydrog. Energy* **2014**, *39*, 14334–14341. [CrossRef]
30. Gryaznov, D.; Baumann, S.; Kotomin, E.A.; Merkle, R. Comparison of permeation measurements and hybrid density-functional calculations on oxygen vacancy transport in complex perovskite oxides. *J. Phys. Chem. C* **2014**, *118*, 29542–29553. [CrossRef]
31. Neuhaus, K.; Eickholt, S.; Maheshwari, A.; Schulze-Küppers, F.; Baumann, S.; Wiemhöfer, H.-D. Analysis of charge transport in $Ce_{0.8}Gd_{0.2-x}PrxO_{2-\delta}$ at $t \leq 600$ °C. *J. Electrochem. Soc.* **2017**, *164*, H491–H496. [CrossRef]